Journal of Environmental Chemical Engineering 12 (2024) 113470

Contents lists available at ScienceDirect

Journal of Environmental Chemical Engineering

journal homepage: www.elsevier.com/locate/jece

Study of pyrene-based covalent organic frameworks for efficient photocatalytic oxidation of low-concentration NO

Zhiyu Xiao [a], Yong Ren [b], George Zheng Chen [c], Yong Sun [a], Chengjun Wang [d], Jun He [a,e,*]

[a] Department of Chemical and Environmental Engineering, University of Nottingham Ningbo China, Ningbo, Zhejiang 315100, China
[b] Department of Mechanical, Materials and Manufacturing Engineering, University of Nottingham Ningbo China, Ningbo, Zhejiang 315100, China
[c] Department of Chemical and Environmental Engineering, University of Nottingham, Nottingham NG7 2RD, UK
[d] College of Resources and Environmental Sciences, South-Central Minzu University, Wuhan, Hubei 430074, China
[e] Nottingham Ningbo China Beacons of Excellence Research and Innovations Institute, Ningbo, Zhejiang 315032, China

ARTICLE INFO

Keywords:
Chemically bonded heterostructure
Covalent organic framework
In-Situ Growth
Photocatalytic NO removal
Graphitic carbon nitride

ABSTRACT

This research presents the development of innovative pyrene-based COFs aimed at enhancing photocatalytic oxidation of low-concentration nitrogen oxide. By precisely modifying the structural length and incorporating additional functional groups into pyrene-based COFs, we identified TAPPy-DMTP-COF as the most effective performer. This COF, characterized by its shortest length and the presence of -OCH_3 functional groups, demonstrated superior performance, likely due to reduced electron transfer resistance and the presence of additional oxygen active sites. Building on the potential of TAPPy-DMTP-COF, we developed a covalently linked Type-II heterostructure with g-C_3N_4. The resulting heterostructure, 40TAPPy-DMTP-COF/g-C_3N_4, with a 40 % mass fraction of TAPPy-DMTP-COF, was confirmed using SEM, XRD, and other techniques. It exhibited an exceptional photocatalytic efficiency of 45.8 % and NO_3^- selectivity of 97.4 %. This remarkable performance can be attributed to improved electron communication facilitated by chemical bonding, as confirmed by XPS results. Additionally, the optimized heterostructure interface not only improved electron transfer but also inhibited the recombination of electron-hole pairs. The growth of TAPPy-DMTP-COF on the surface of g-C_3N_4 significantly enhanced visible light absorption, as confirmed by UV–vis spectroscopy. This study not only underscores the importance of precise control over the structural features of pyrene-based COFs but also introduces a novel approach for enhancing NO oxidation. By constructing a covalently linked Type-II heterostructure, we have significantly enhanced the interface interaction within the heterostructure, leading to superior photocatalytic performance.

1. Introduction

Environmental pollution, particularly from nitrogen oxides (NO_x), remains a major global challenge due to its adverse impact on air quality, human health, and ecosystems. Innovative materials for the photocatalytic oxidation of NO_x are critical for sustainable environmental remediation strategies. Covalent organic frameworks (COFs), a class of porous crystalline materials, have attracted significant attention recently owing to their exceptional structural diversity, tailor-ability, and stability [1,2]. Constructed from organic building blocks linked by strong covalent bonds, COFs exhibit a wide range of functional properties making them suitable for various applications including gas storage, separation, catalysis, and photocatalysis [3,4]. The designable nature of COFs enables precise manipulation of their pore sizes, surface areas, and functional groups, offering a unique platform for exploring novel photocatalytic materials [5].

Within the realm of advanced photocatalytic materials, pyrene-based COFs have emerged as a prominent class of crystalline porous polymers, offering a spectrum of beneficial features [6,7]. Their well-defined and modifiable structures enable precise tuning of physical and chemical properties. Notably, pyrene-based COFs, which incorporate pyrene moieties demonstrate extended π-conjugation and robust electronic interactions, facilitating exceptional electron delocalization and transport [8]. This enhances the capture and conversion of light energy, making them ideal for composite photocatalytic systems. Additionally, their high surface areas and the capacity for functional group modification

* Corresponding author at: Department of Chemical and Environmental Engineering, University of Nottingham Ningbo China, Ningbo, Zhejiang 315100, China.
E-mail address: jun.he@nottingham.edu.cn (J. He).

https://doi.org/10.1016/j.jece.2024.113470
Received 25 April 2024; Received in revised form 25 June 2024; Accepted 30 June 2024
Available online 1 July 2024

improve the adsorption and transformation of environmental pollutants [9]. The π–π stacking of the pyrene layers in the Z-direction enhances the conjugation within COFs and lowers the band gap, while their 2D layered structures provide a robust platform for tailoring photocatalytic properties through molecular engineering [10]. Recent studies on pyrene-based COFs have demonstrated their efficacy in photocatalytic H_2O_2 and H_2 production, showing that optimized surface areas and modifications with nitrogen and bromine atoms significantly impact performance. Larger surface areas were found to induce higher H_2O_2 production due to the increased number of active sites [7]. Moreover, carbon atoms adjacent to bromine atoms reduced the energy barrier for photocatalytic H_2 production. Conversely, modifications with nitrogen atoms led to a significant decrease in efficiency due to an increased thermodynamic driving force [11,12]. The precise control of COF features is crucial for enhancing photocatalytic reactions. However, many aspects remain unexplored, such as modifications with other atoms or functional groups and variations in unit length. These unexplored avenues highlight the immense potential of pyrene-based COFs in photocatalytic applications, particularly for the efficient oxidation of low-concentration NO.

Graphitic carbon nitride (g-C_3N_4), with its graphite-like structure and semiconductor properties, is recognized as a promising candidate for photocatalytic applications, chiefly due to its suitable band gap for visible light absorption, excellent thermal and chemical stability, and straightforward synthesis from inexpensive precursors [13]. However, its effectiveness is often limited by a high recombination rate of photo-induced electron-hole pairs and a constrained surface area for NO adsorption. Consequently, various strategies have been explored to modify g-C_3N_4 and mitigate these limitations. Vacancy engineering and the fabrication of heterostructures have been investigated to enhance the photocatalytic efficiency of g-C_3N_4 for NO oxidation. Carbon and nitrogen vacancies serve as active sites and electron trapping sites, which increase NO adsorption and inhibit electron-hole pair recombination, respectively [14,15]. Heterostructure engineering, in particular, has attracted considerable attention due to its simpler synthesis procedures and diverse configurations. The formation of heterostructures not only facilitates the separation of photogenerated carriers but also provides additional active centers for the photocatalytic oxidation of NO [16,17]. Nevertheless, the construction of heterostructures cannot completely suppress the recombination of electron-hole pairs, as it is limited by the weak interactions between materials due to Van der Waals forces [18]. Therefore, optimizing the heterostructure interface or modifying the type of linkage within the heterostructure presents a potential approach to ensure a seamless interface between materials. This, in turn, would foster strong intermolecular interactions and create an efficient charge transfer pathway.

In this study, we synthesized three variants of pyrene-based COFs—1,3,6,8-tetrakis-(p-aminophenyl)-pyrene with terephthalaldehyde (TAPPy-TPA-COF), 1,3,6,8-tetrakis-(p-aminophenyl)-pyrene with 2,5-dimethoxybenzene-1,4-dicarboxaldehyde (TAPPy-DMTP-COF), and 1,3,6,8-tetrakis-(p-aminophenyl)-pyrene with 4,4'-Biphenyldicarboxaldehyde (TAPPy-BPDA-COF)—to assess the impact of structural variations on photocatalytic efficiency. As shown in Fig. 1, TAPPy-TPA-COF, with a shorter structural length but lacking a C-O-C bond, and TAPPy-BPDA-COF, with a longer length and no C-O-C bond, were compared with TAPPy-DMTP-COF, which features both a shorter length and an additional C-O-C bond. Our comparative analysis revealed that TAPPy-DMTP-COF exhibited the highest efficiency, leading to its selection for further development. Subsequently, TAPPy-DMTP-COF was integrated with g-C_3N_4 using an in-situ growth method to create a chemically linked heterostructure. This structure promotes a stronger interfacial driving force and larger contact area, enhancing electron communication between TAPPy-DMTP-COF and g-C_3N_4. Additionally, the porous structure of TAPPy-DMTP-COF, strategically designed on the g-C_3N_4 surface, boosts the adsorption of both NO and light, crucial for improving the photocatalytic oxidation of NO. The in-situ growth approach not only ensures a robust interface between the COFs and g-C_3N_4 but also enhances interfacial charge transfer, providing a pathway

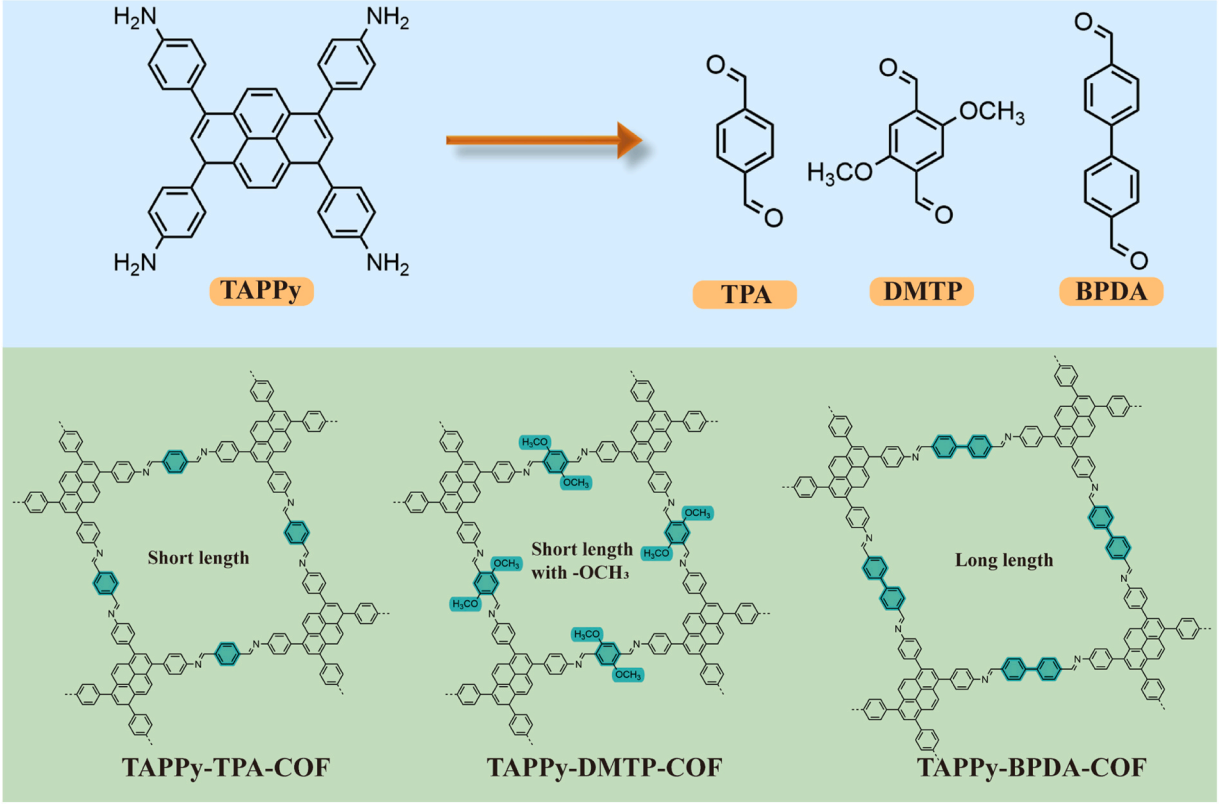

Fig. 1. Structure of TAPPy-TPA-COF, TAPPy-DMTP-COF and TAPPy-BPDA-COF.

for advanced photocatalytic oxidation of NO.

2. Materials and methods

2.1. Preparation of photocatalysts

Nanosheet g-C_3N_4(CN): Nanosheets CN were synthesized following an established method [13]. 4 g of melamine were heated in a covered alumina crucible at 550°C for 4 h in a muffle furnace. The resulting calcined product was then ground into a fine powder for subsequent use.

TAPPy-DMTP-COF: Synthesis commenced with the mixing of 28.33 mg of 1,3,6,8-tetrakis-(p-aminophenyl)-pyrene (TAPPy) (0.05 mmol) and 19.41 mg of 2,5-dimethoxybenzene-1,4-dicarboxaldehyde (DMTP) (0.1 mmol) in a 10 mL Pyrex tube. The mixture was then dissolved in 1.5 mL of N, N-Dimethylacetamide (DMAc) and 0.5 mL of o-Dichlorobenzene (o-DCB), followed by adding of 0.2 mL acetic acid (6 mol/L) and ultrasonication for 30 min at room temperature. After undergoing three freeze-pump-thaw cycles, the tube was heated to 120 °C for 72 h. The resultant COF was washed with tetrahydrofuran, subjected to Soxhlet extraction for 24 h, and finally dried under vacuum at 60 °C.

TAPPy-TPA-COF: Analogous to the TAPPy-DMTP-COF synthesis process, 28.33 mg of TAPPy (0.05 mmol) reacted with 13.41 mg of terephthalaldehyde (TPA) (0.1 mmol) under the identical condition to yield TAPPy-TPA-COF after Soxhlet extraction and drying.

TAPPy-BPDA-COF: Employing the same methodology, 28.33 mg of TAPPy (0.05 mmol) was reacted with 21.02 mg of 4,4'-Biphenyldicarboxaldehyde (BPDA) (0.1 mmol). The subsequent product underwent the same Soxhlet extraction and vacuum drying to obtain TAPPy-BPDA-COF.

TAPPy-DMTP-CN: The synthetic process of TAPPy-DMTP-CN is identical to that of TAPPy-DMTP-CN, with the addition of a specific amount of g-C_3N_4. Various mass fractions of T TAPPy-DMTP-COF were synthesized and denoted as XTAPPy-DMTP-CN (where X represents the mass fraction of TAPPy-DMTP-COF).

2.2. Characterization

A comprehensive array of sophisticated analytical techniques was utilized to delineate the structural, morphological, and electronic characteristics of the synthesized catalysts. The following methods were employed for detailed characterization:

X-ray Diffraction (XRD) Analysis: Crystalline structures were analyzed using a Bruker D8 Advance diffractometer.

Scanning Electron Microscopy (SEM): Surface morphologies were visualized with a ZEISS Sigma 500 microscope.

X-ray Photoelectron Spectroscopy (XPS): Surface compositions and elemental states were determined using a Thermo K-alpha spectrometer, with spectra calibrated against the C 1 s peak at 284.6 eV to standardize the surface carbon signal.

Electron Paramagnetic Resonance (EPR) Spectroscopy: Electronic spin properties were characterized using a Bruker A300.

UV–Vis Diffuse Reflectance Spectroscopy (UV-Vis-DRS): Optical absorption features were assessed with a Shimadzu UV-3600+ spectrophotometer.

Photoluminescence Spectrum (PL): Emission properties were measured using a HITACHI F-4600 spectrophotometer.

Active species trapping experiment: To explore the roles of reactive species in the photocatalytic degradation process, targeted trapping experiments were conducted. Key reagents, including potassium iodide, potassium dichromate, tert-butanol, and p-benzoquinone, were employed to selectively trap and analyze h^+, e^-, •OH, and $•O_2^-$ species.

The collective results from these analytical endeavors painted a detailed portrait of the catalysts' structural design, surface characteristics, and electronic behavior, offering a well-rounded understanding of their intrinsic properties and photocatalytic efficacy.

2.3. Electrochemical measurements

The electronic properties of the synthesized materials were evaluated using transient photocurrent response analysis and electrochemical impedance spectroscopy, performed on a CHI660E workstation (Shanghai Chenhua, China). This setup involved a standard three-electrode system where the working electrode was made of the photocatalyst material, complemented by a platinum wire as the counter electrode and an Ag/AgCl electrode as the reference. To prepare the working electrode, 10 mg of the photocatalyst was mixed into 1 mL of a deionized water and ethanol solution, to which 50 μL of Nafion solution was added. The mixture underwent ultrasonic agitation for 30 min to form a homogenous catalyst ink. This ink was subsequently applied to a fluorine-doped tin oxide (FTO) coated glass and dried under an infrared lamp at room temperature. For the photocurrent and impedance tests, the system was exposed to a 300 W xenon lamp, using a 0.1 M Na_2SO_4 solution as the electrolyte.

2.4. Catalytic activity test

The catalytic performance of the synthesized catalysts for the photocatalytic oxidation of NO was evaluated in a continuous flow cube reactor constructed from quartz. The reactor measured 20 cm×15 cm x 10 cm and was wrapped in aluminum foil on all sides except the top to eliminate external light interference. During the preparation phase, 0.2 g of the catalyst was dispersed in 15 mL of deionized water and ultrasonicated for 15 min to achieve a uniform slurry. This slurry was spread across a 12 cm diameter glass dish and dried under vacuum at 60 °C for 6 h. The catalyst, positioned at the center of the reactor, was activated by a 300 W Xenon lamp fitted with a 420 nm cutoff filter placed 20 cm above the catalyst to ensure even irradiation. The photocatalytic reaction commenced once an adsorption-desorption equilibrium was established between the catalyst and NO gas. The gas stream for the reaction contained 800 ppb NO, diluted from 50 ppm NO with pure air, and was maintained at a flow rate of 2 L/min over the catalyst. NO and NO_2 concentrations were continuously monitored in real-time using an advanced NO_x analyzer (API-T200, USA), allowing precise tracking of reaction kinetics. The efficiency of NO removal via photocatalysis was determined using the following equation:

$$\varphi = \frac{C_0 - C}{C_0} \times 100\% \quad (1)$$

where C_0 (in ppb) is the initial NO concentration and C (in ppb) is the NO concentration at a given time point during the reaction.

2.5. DFT calculation details

We used the DFT as implemented in the Coupled-Cluster Perturbation Theory with the Kernel (CP2K) in all calculations [19]. Calculations were performed at both the generalized gradient approximation (GGA) level, using the Perdew–Burke–Ernzerhof (PBE) functional, and the hybrid density functional theory (DFT) level, which incorporates Hartree–Fock exchange. Structural optimization was performed at the PBE level utilizing DZVP-MOLOPT-SR-GTH basis sets and enhanced with D_3(BJ) dispersion corrections. The calculations maintained a fixed plane-wave cutoff energy of 600 eV and a convergence threshold for the electronic energy was meticulously set at 10^{-5} eV. The Gamma point was considered during calculation for precision.

3. Results and discussion

3.1. Catalyst characterization

In this study, CN was incorporated into a specified mixture containing TAPPy and DMTP, along with selected organic solvents. Through

a targeted Schiff base reaction, TAPPy-DMTP-COF was synthesized preferentially on the surface of the CN nanosheets, facilitating in-situ growth. This process is illustrated in Fig. 2(a), which highlights the precise formation of the composite material.

The phase structures of CN, TAPPy-DMTP-COF, and TAPPy-DMTP-CN were thoroughly investigated using powder X-ray diffraction (PXRD) analysis. The PXRD patterns, shown in Fig. 2(b), align remarkably well with the simulated results in DFT calculation, indicating minimal structural variation and confirming the successful synthesis of the AA-stacking structure of TAPPy-DMTP-COF [20]. Specifically, the TAPPy-DMTP-COF displayed characteristic peaks at 3.9°, 4.8°, and 7.7°, which correspond to the (100), (110), and (001) facets, respectively. Moreover, It was observed that the PXRD pattern of CN closely aligned with the reference pattern for CN (PDF 87–1526#), indicating the retention of its structural integrity [21]. Further investigations extended to a composite sample, TAPPy-DMTP-CN, with its PXRD patterns compared alongside those of pure CN and TAPPy-DMTP-COF, as presented in Fig. 2(c). Significantly, the composite's PXRD patterns displayed peaks from both COF and CN components, indicating that the integration process preserved the structural integrity of both materials. Consequently, the PXRD results unequivocally confirm the successful synthesis of the TAPPy-DMTP-CN composite. The observed structural stability after integration underscores the effectiveness of the in-situ growth method in preserving the inherent structures of TAPPy-DMTP-COF and CN, thereby facilitating the formation of a binary heterostructure with promising photocatalytic potential as demonstrated in Section 3.3.

FT-IR spectroscopy results revealed distinctive transmittance peaks across the samples. As depicted in Fig. 2(d), the spectra for CN, TAPPy-DMTP-COF, and 40TAPPy-DMTP-CN were largely similar. All spectra displayed broader transmittance in the 3100–3700 cm^{-1} region, likely corresponding to N-H stretching vibrations from amine or amide groups, indicative of hydrogen-bonding interactions [22]. A notable peak at 1576 cm^{-1} was attributed to C═C stretching vibrations typical of aromatic compounds, while a peak around 1285 cm^{-1} suggested C-N stretching vibrations characteristic of aromatic amines. Additionally, a distinct peak at 1644 cm^{-1} aligned with C═N stretching vibrations, commonly found in Schiff bases or imine compounds [23]. These findings confirm the presence of graphitic and aromatic nitrogenous compounds in the synthesized materials and highlights the successful integration of CN with the newly synthesized TAPPy-DMTP-COF to form the TAPPy-DMTP-CN composite.

SEM analysis revealed distinct morphological features of synthesized samples. The SEM image in Fig. 3(a) displayed CN's typical smooth nanosheet structures, indicating a homogeneous crystalline structure, confirming successful synthesis [24]. In contrast, Fig. 3(b) revealed a markedly different morphology for TAPPy-DMTP-COF, characterized by numerous clusters. After the in-situ growth of TAPPy-DMTP-COF on CN, Fig. 3(c) highlighted the composite material's hybrid structure, with clusters of TAPPy-DMTP-COF grown on the smooth nanosheets of CN.

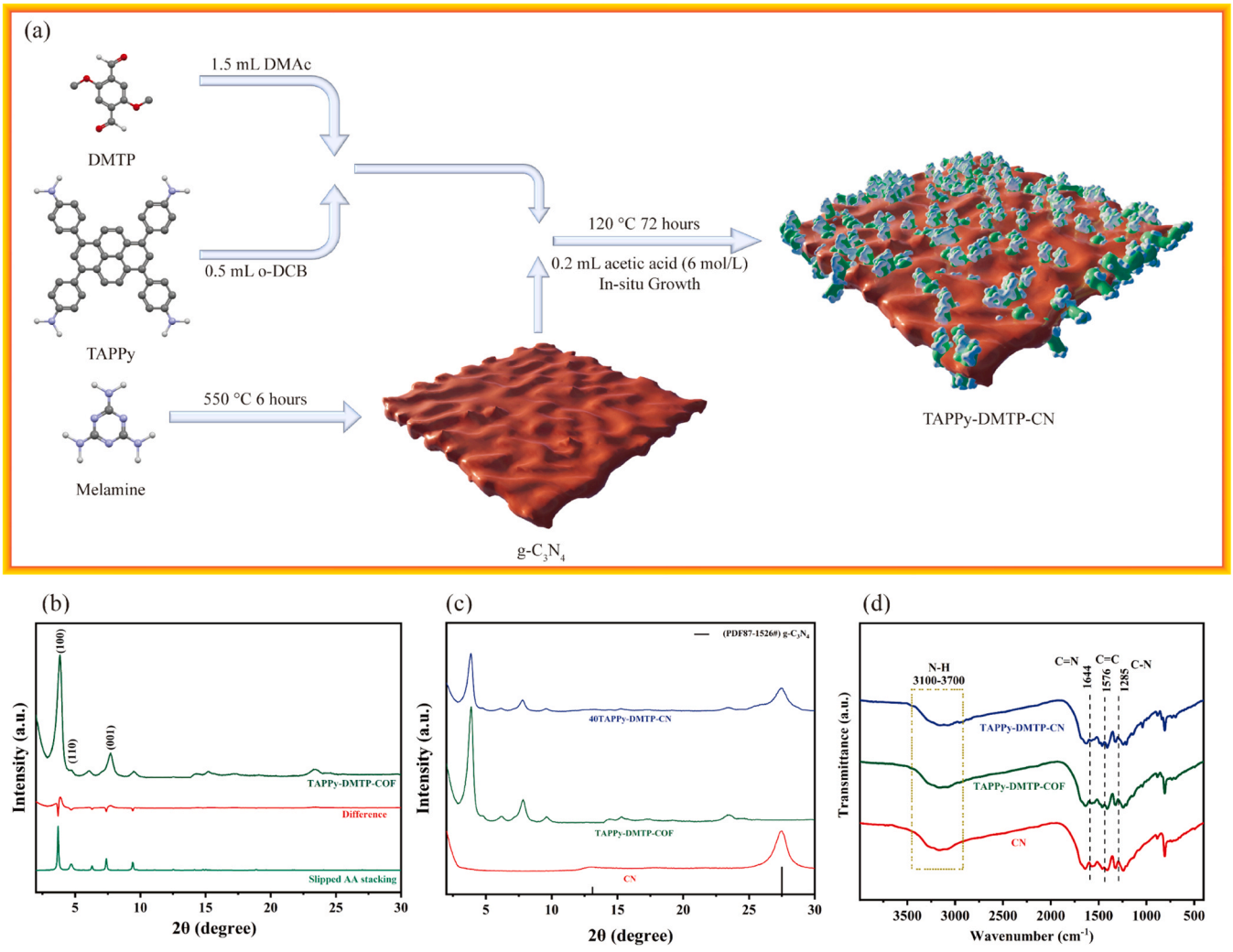

Fig. 2. (a) synthesis procedure illustration, (b) experimental and simulated PXRD pattern of TAPPy-DMTP-COF, (c) PXRD patterns and (d) FT-IR results of CN, TAPPy-DMTP-COF and 40TAPPy-DMTP-CN.

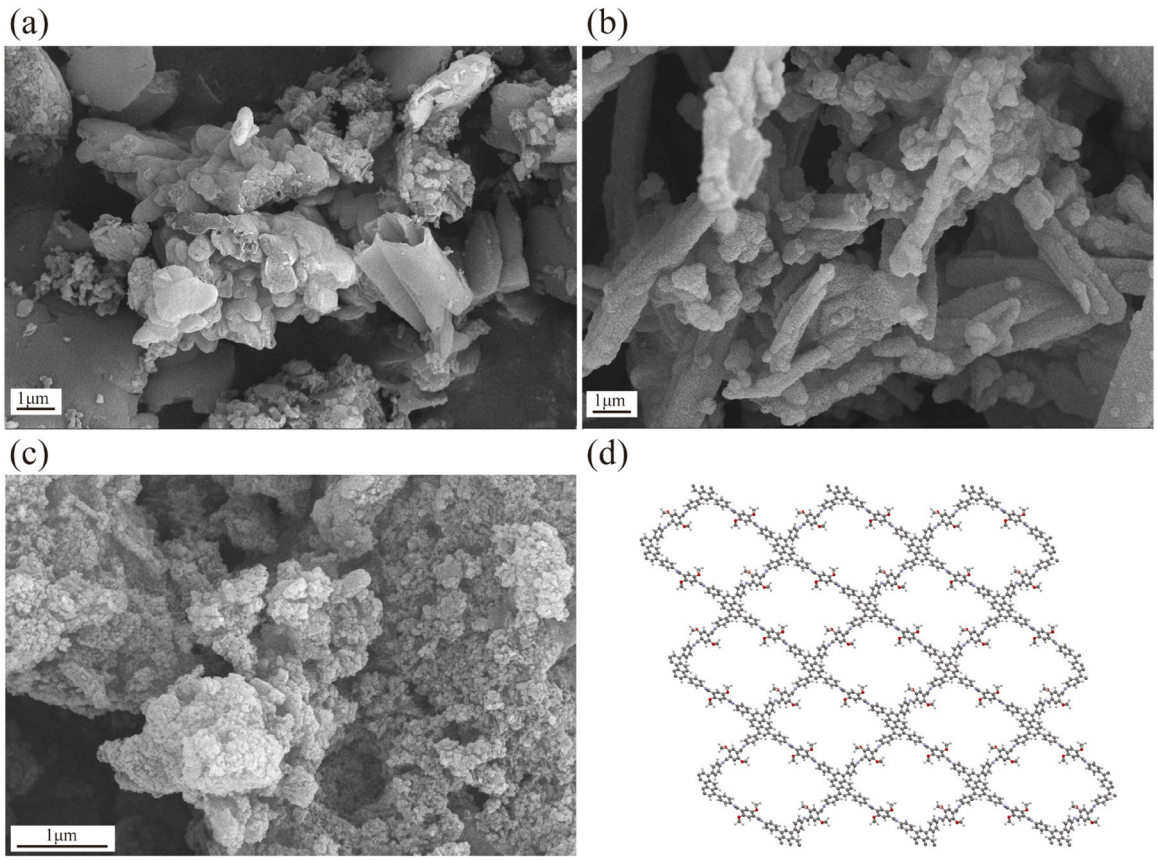

Fig. 3. SEM results of (a) CN, (b) TAPPy-DMTP-COF, (c) 40TAPPy-DMTP-CN and (d) structure of TAPPy-DMTP-COF.

This interfacing suggests successful heterojunction formation, potentially providing a synergistic effect beneficial for photocatalytic activity due to improved charge separation and transfer at the interface. The SEM images provide strong evidence of the successful synthesized of TAPPy-DMTP-CN, preserving the crystal structure and indicating possible interaction between the components.

The XPS analysis provided insights into the electronic environment of the elements within the samples. The C1s spectrum in Fig. 4(a) shows distinct peaks at 284.8 eV, associated with C-C bonding typical of CN, and at 286.2 eV, attributable to C-N bonds in TAPPy-DMTP-COF [25, 26]. In the composite TAPPy-DMTP-CN, the peak corresponding to TAPPy-DMTP-COF shifted slightly to lower energy, indicating an alteration in the electronic structure, suggestive of charge transfer between CN and TAPPy-DMTP-COF. Additionally, the presence of a peak at 288.2 eV in both CN and TAPPy-DMTP-CN indicates a shift towards higher energy for the N-C═N bond post-integration, confirming the interaction that potentially facilitate electron transfer from CN to COF. The N1s spectrum, shown in Fig. 4(b), features peaks at 398.5 eV assigned to C-N═C in CN, TAPPy-DMTP-COF and TAPPy-DMTP-CN, indicating the formation of C-N═C via Schiff-base reactions during COF synthesis. In CN sample, peaks at 399.2 eV, 400.9 eV and 404.2 eV correspond to N-$(C)_3$ bond, C-NH_x bond and π-π excitation, respectively [27]. For TAPPy-DMTP-COF, the peak at 400.1 eV suggests the existence of C-N bonds [11]. This peak shifts towards lower energy in the composite after in-situ growth of the COF on g-C_3N_4, indicating electron transfer from CN to COF, consistent with the C 1 s spectrum. Regarding the O 1 s spectra in Fig. 4(c), a peak at 532.1 eV in CN is attributed to surface-adsorbed oxygen species. For TAPPy-DMTP-COF and TAPPy-DMTP-CN, a new peak observed at 533.4 eV, a new peak at 533.4 eV is observed, likely corresponding to oxygen-containing functional groups in the COF such as O-CH_3 [13]. In summary, the XPS results not only confirm the successful synthesis of the TAPPy-DMTP-COF and its composite with CN but also suggest significant electronic interaction between these materials. This interaction is crucial for enhancing photocatalytic performance due to the formation of a functional heterostructure.

3.2. Photoelectrochemical properties and band structure

The synthesized materials were extensively characterized using various spectroscopic and electrochemical techniques to elucidate their photophysical and photoelectrochemical properties. UV-Vis spectroscopy, which measures the absorption of ultraviolet or visible light by a substance, revealed the electronic structure of the materials. In the UV-Vis spectra shown in Fig. 5(a), CN exhibited a strong absorption band around 320 nm. This band was red-shifted in TAPPy-DMTP-COF, suggesting alterations in electronic structure. Additionally, the composite 40TAPPy-DMTP-CN showed an absorption profile that combined features of both CN and TAPPy-DMTP-COF, with a further noticeable red shift suggesting a smaller bandgap likely due to the formation of a heterojunction [28]. This shift suggests enhanced light absorption capabilities possibly induced by the in-situ growth of TAPPy-DMTP-COF on the surface of CN.

PL spectroscopy, which measures the light emission as electrons return to their ground state after excitation, was used to assess the recombination dynamics of the photocatalysts. Fig. 5(b) illustrated the PL spectra of the synthesized photocatalysts, excited at a 370 nm emission wavelength under room temperature conditions. Notably, g-C_3N_4 demonstrated the highest fluorescence emission, indicating significant electron-hole recombination under illumination [29]. However, the 40TAPPy-DMTP-CN composite showed the lowest peak intensity, confirming that the integration of CN and 40TAPPy-DMTP-COF effectively reduced the recombination rate of electrons and holes, likely due to formation of heterostructure.

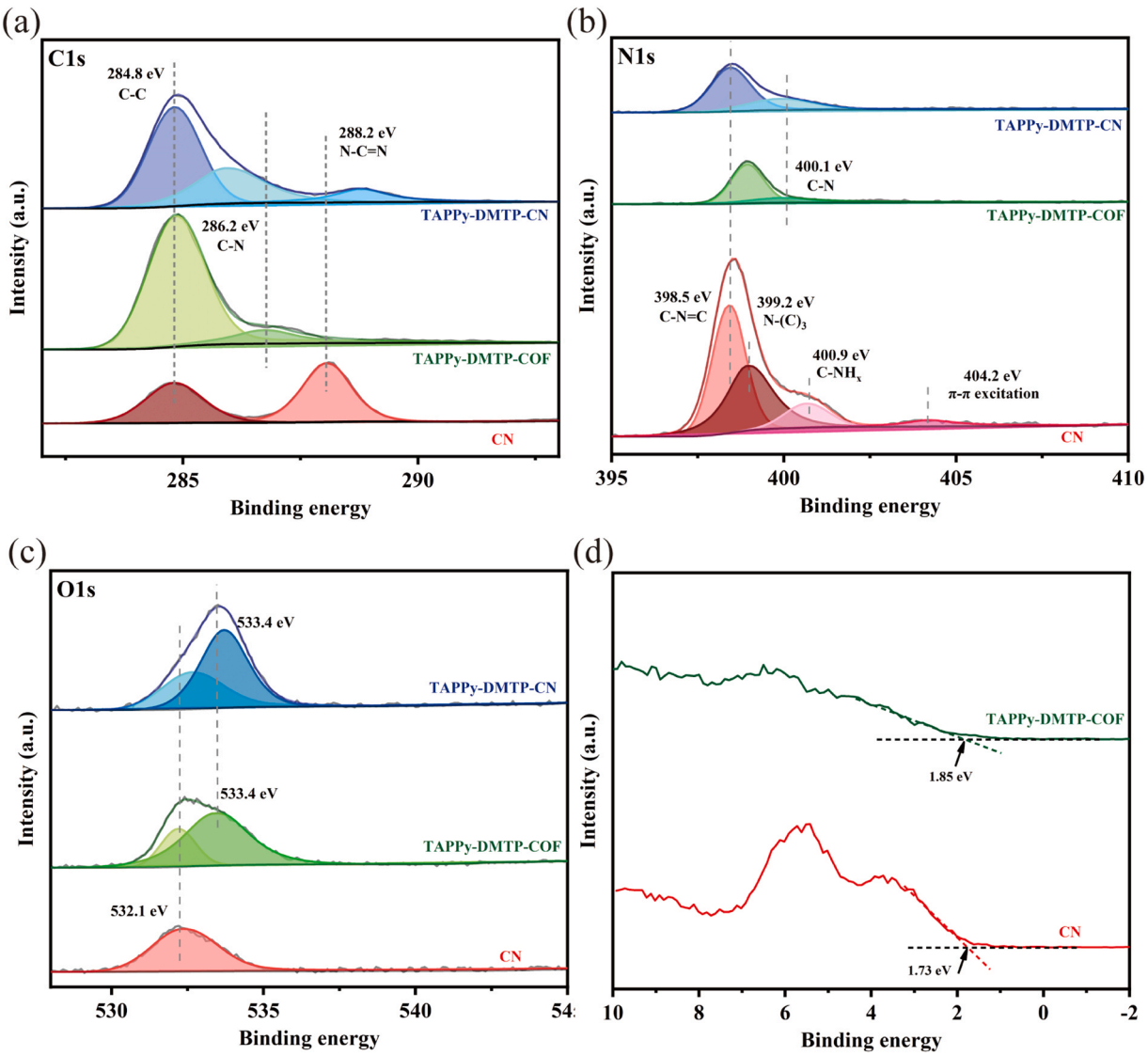

Fig. 4. XPS spectra of CN, TAPPy-DMTP-COF and 40TAPPy-DMTP-CN for (a) C 1 s, (b) N 1 s and (c) O 1 s, (d) XPS-VB of CN and TAPPy-DMTP-COF.

Transient photocurrent response and EIS analysis were performed to further explore the photoelectrochemical properties of synthesized photocatalyst. These techniques assesses the generation and recombination of charge carriers and the resistance of a material to charge transfer, respectively. Fig. 5(c) revealed a significantly higher photocurrent for the 40TAPPy-DMTP-CN composite compared to individual TAPPy-DMTP-COF and CN, evidencing superior separation and migration efficiency of photogenerated charge carriers. This enhanced photoconductivity and effective charge separation were corroborated by PL spectroscopy findings. Furthermore, EIS Nyquist plots in Fig. 5(d) indicated that the 40TAPPy-DMTP-CN composite had the smallest semicircle diameter, implying the lowest charge transfer resistance among the tested materials [30]. This implies more efficient charge transfer process at the electrode-electrolyte interface, consistent with enhanced separation of charge carriers observed in the photocurrent analysis.

To further elucidate the photocatalytic mechanism of these samples, Tauc plot were employed to estimate the bandgap energies of as-prepared samples, based on Kubelka-Munk equation [31]:

$$(\alpha h\nu)^{\frac{1}{n}} = A(h\nu - E_g) \quad (2)$$

where α is the optical adsorption coefficient, $h\nu$ represents the absorption energy, Eg is the band gap, and n is equal to 1/2 in this experiment. As revealed in Fig. 5(e), the bandgap energies for CN, TAPPy-DMTP-COF, and 40TAPPy-DMTP-CN are approximately 2.80 eV, 2.33 eV, and 2.25 eV, respectively [32]. This reduction in bandgap within the composite material indicates a modified electronic structure that enhances visible light absorption and photocatalytic activity for NO degradation. Meanwhile, XPS valence band analysis was employed to obtain the complete band structure of as-prepared samples. The valence band maximum (VBM) obtained from XPS indicates the energy position of the highest occupied electronic state. The XPS-VB result in Fig. 4(d) indicates the top of the valence band (VBs) for CN and TAPPy-DMTP-COF positioned at 1.73 eV and 1.85 eV, respectively, below the Fermi level. Thus, the conduction band (CBs) of g-C_3N_4 and TAPPy-DMTP-COF are −1.07 eV and −0.48 eV, respectively [33].

Consequently, the UV-Vis absorption spectra, bandgap estimation from Tauc plots, valence band analysis from XPS, PL spectroscopy, transient photocurrent response, and EIS Nyquist plots collectively suggest that the 40TAPPy-DMTP-CN composite material exhibits superior optical properties, enhanced charge separation, and reduced recombination of charge carriers compared to its individual components. These attributes are highly implied that the integration of CN and TAPPy-DMTP-CN has effectively modified the electronic structure, enhancing photocatalytic performance through the formation of

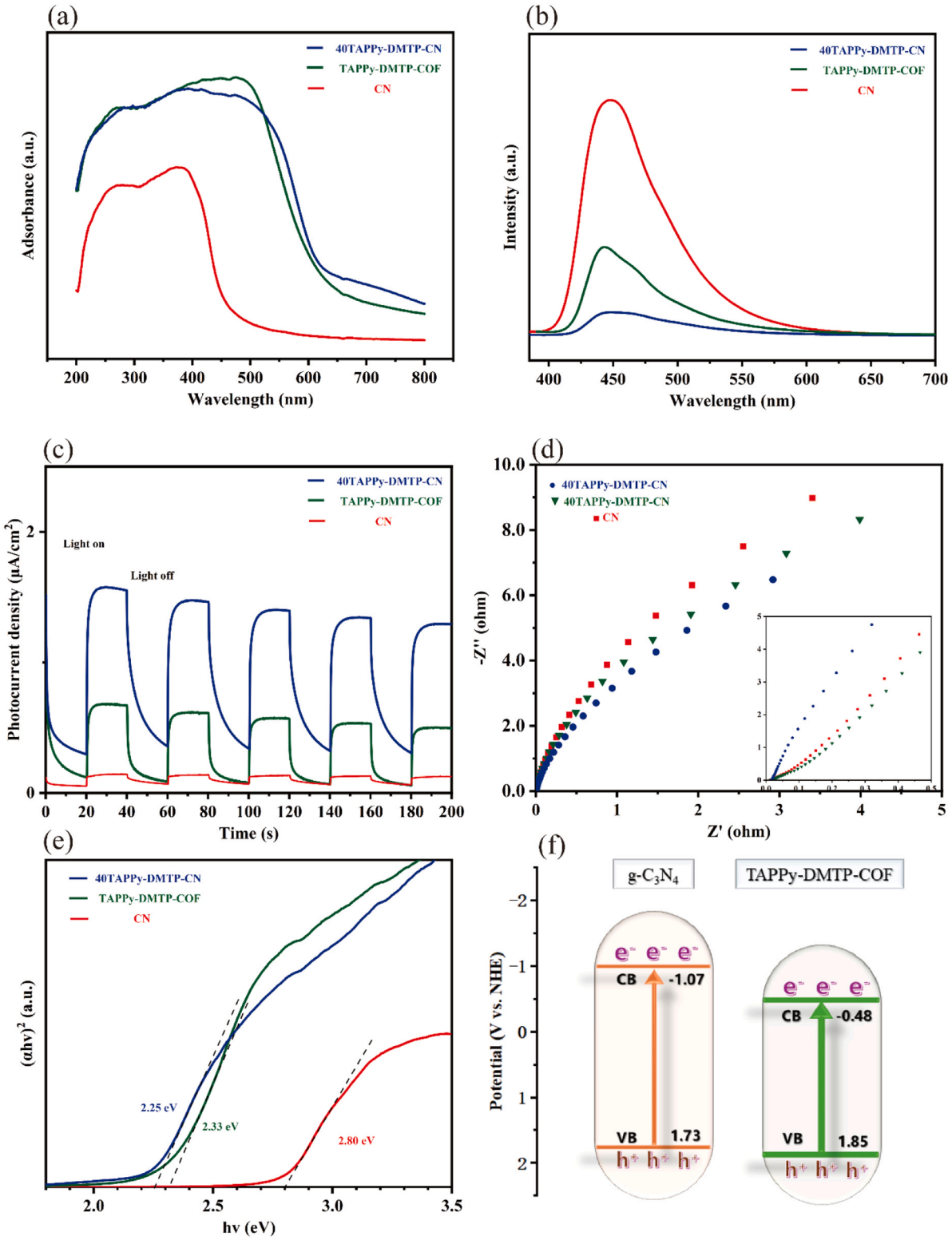

Fig. 5. (a) PL results, (b) Uv-vis spectroscopy, (c) transient photocurrent response curves, (d) EIS plots, (e) bandgap and (f) band structure of CN, TAPPy-DMTP-COF and 40TAPPy-DMTP-CN.

heterostructure. Furthermore, the band structure of CN and TAPPy-DMTP-COF were obtained by XPS-VB and UV–vis which is shown in Fig. 5(f).

3.3. Photocatalytic activity tests

In this study, we evaluated the photocatalytic oxidation efficiency of NO using a series of pyrene-based COFs designed to optimize the structure for achieve an optimal COF-CN photocatalyst. The series comprised COFs synthesized with TAPPy as the amine monomer and

DMTP, TPA, and BPDA as the aldehyde monomers, forming a spectrum of 2D COFs with varying structural lengths and extra functional groups. Fig. 6(a), demonstrates that TAPPy-DMTP-COF, characterized by the shortest structural length and a C-O-C linkage, exhibited the highest photocatalytic performance, achieving the greatest efficiency in NO oxidation. This enhanced performance can be attributed to shorter electron transfer pathways within the COF, which facilitate rapid electron transport and minimize recombination losses. Additionally, the incorporation of oxygen atoms within C-O-C linkages likely improves the photocatalytic activity, as these atoms may serve as active sites for adsorption and oxidation of NO. Conversely, elongating the COF structure, as seen with TAPPy-TPA-COF and TAPPy-BPDA-COF, resulted in a noticeable decline in photocatalytic activity. This observation suggests that COF structures may introduce kinetic barriers to electron transport, thus mitigating the photocatalytic reaction efficiency.

The integration of CN with the previously optimized TAPPy-DMTP-COF was performed to explore synergistic effects on the photocatalytic oxidation efficiency of NO. As shown in Fig. 6(b), pure g-C_3N_4

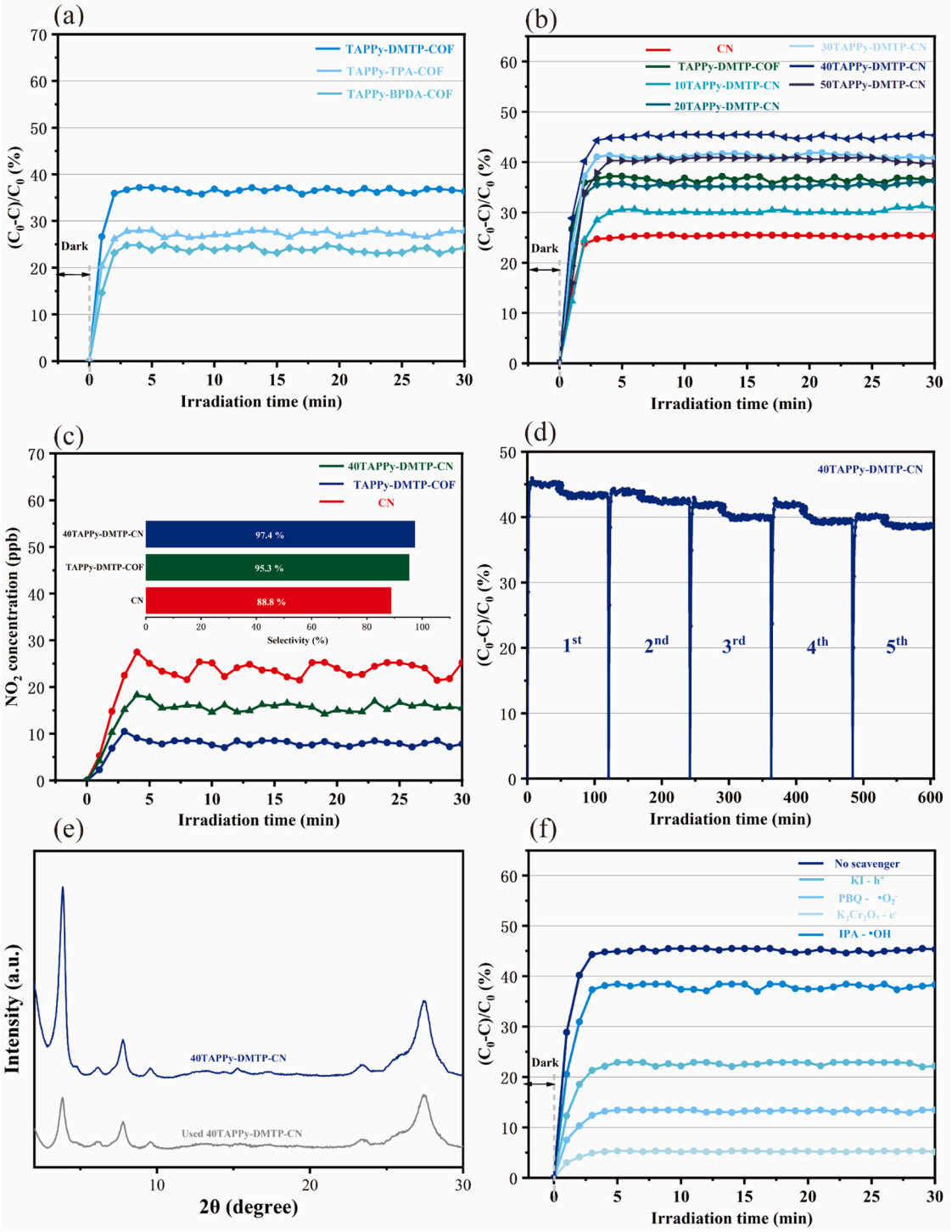

Fig. 6. (a) Efficiency comparison between TAPPy-DMTP-COF, TAPPy-TPA-COF and TAPPy-BPDA-COF and (b) TAPPy-DMTP-CN with different mass fraction of TAPPy-DMTP-COF. (c) The selectivity of CN, TAPPy-DMTP-COF and 40TAPPy-DMTP-CN, (d) cycle experiment result of 40TAPPy-DMTP-CN, (e) PXRD results of 40TAPPy-DMTP-CN before and after reaction, (f) trapping experiment results of 40TAPPy-DMTP-CN.

demonstrated a baseline photocatalytic efficiency of 25.1 %, while TAPPy-DMTP-COF alone reached an efficiency of 38.2 %. The subsequent amalgamation of TAPPy-DMTP-COF onto CN resulted in a composite material with photocatalytic efficiency surpassed each individual component, reaching 45.8 % at a 40 % mass fraction of TAPPy-DMTP-COF. This significant increase is attributed to robust interaction between TAPPy-DMTP-COF and CN, which enhance charge separation and transfer, as supported by photoelectrochemical measurements. The efficiency enhancement up to the 40 % loading threshold suggests an optimal distribution of TAPPy-DMTP-COF over the CN surface, providing a balance between active sites exposure and effective charge carrier dynamics. Contrarily, a mass fraction increase beyond 40 % led to a decline in efficiency. This phenomenon is likely due to the aggregation of excessive TAPPy-DMTP-COF, which could obstruct the interaction interface between the components, consequently hindering the crucial charge transfer processes. Consequently, the 40 % TAPPy-DMTP-COF in CN composite (40TAPPy-DMTP-CN) emerged as the most efficient photocatalyst. Compared to previous g-C_3N_4-based photocatalysts, 40TAPPy-DMTP-CN exhibits relatively higher efficiency, highlighting its strong potential for the photocatalytic oxidation of NO through the in-situ growth of COF on nanosheet g-C_3N_4. The chemically bonded composite not only optimizes the heterostructure interface between g-C_3N_4 and TAPPy-DMTP-CN but also provides porous structure for active site on g-C_3N_4, facilitating a better photocatalytic performance. However, the absence of metal elements acting as active sites results in lower photocatalytic efficiency compared to Bi-based photocatalysts, as shown in Table 1. This discrepancy arises from the different photocatalytic mechanisms involving metal active sites, suggesting a potential pathway for further improvement of TAPPy-DMTP-CN by doping metal active sites.

A pivotal aspect of evaluating photocatalyst performance is assessing selectivity, particularly in the context of NO degradation, where the formation of nitrates (NO_3^-) is desirable. The selectivity investigation, illustrated in Fig. 6(c), demonstrates that the composite 40TAPPy-DMTP-CN not only performs best in photocatalytic efficiency but also exhibits superior selectivity towards NO_3^- formation. Upon irradiation, CN displayed a selectivity of 83.8 %, indicating its propensity for converting NO/NO_2 to NO_3^-. TAPPy-DMTP-COF, with inherently higher photocatalytic activity, exhibited an enhanced selectivity of 95.3 %. Remarkably, the selectivity was further augmented to 97.4 % with the 40TAPPy-DMTP-CN composite. The high selectivity of the composite suggests an effective suppression of competitive side reactions, thereby directing the photocatalytic pathway towards nitrate production. This enhancement in selectivity can be attributed to the cooperative interactions within the composite, where the TAPPy-DMTP-COF component likely provides additional active sites for the selective adsorption and conversion of NO_2. Moreover, the charge carrier dynamics facilitated by the intimate interface between TAPPy-DMTP-COF and CN may play a role in the improved selectivity, with heterostructure formation ensuring sufficient photogenerated electron participate in photocatalytic reaction.

Long-term operational stability is a benchmark for the practical application of photocatalysts. As presented in Fig. 6(d), the photostability of the 40TAPPy-DMTP-CN composite was rigorously evaluated over a continuous 600-minute irradiation cycle. The results reveal a marginal decrease in photocatalytic efficiency, from an initial 45.8–40.8 %, after five successive cycles. This less than 5 % decline signifies the robustness of the composite, asserting its potential for prolonged use in photocatalytic oxidation of NO. Throughout the cycling tests, 40TAPPy-DMTP-CN maintained remarkably consistent photocatalytic performance, underscoring the durability of the COF-CN interface and the structural integrity of the composite under extensive photo-irradiation. The minor reduction in efficiency may be attributed to unavoidable deactivation phenomena such as gradual fouling of active sites by NO_3^- or the slight detachment of the COF from the CN substrate. Furthermore, the comparative XRD analysis of 40TAPPy-DMTP-CN before and after the photocatalytic cycling experiment, as depicted in Fig. 6(e), reveals no discernible changes in the diffraction patterns, substantiating the high stability of the composite. The consistent position and intensity of the diffraction peaks indicate that the structural integrity is maintained even after repeated catalytic cycles. This preservation of crystallinity suggests that the composite is not subject to significant deactivation or structural degradation under the conditions tested, underscoring its potential for practical applications in photocatalytic NO degradation, where material robustness is crucial for long-term operation.

3.4. NO photocatalytic oxidation mechanism

To delineate the photocatalytic oxidation mechanism of NO, radical trapping experiments were conducted using various scavengers: KI for h^+ trapping, PBQ for $\bullet O_2^-$ radical trapping, $K_2Cr_2O_7$ for e^- trapping, and IPA for •OH radical trapping, as represented in Fig. 6(f). The influence of each reactive oxygen species (ROS) on the photocatalytic oxidation of NO was quantitatively assessed to ascertain the predominant active species in the process [14]. The experimental results reveal a significant role for photogenerated electrons, as evidenced by the substantial decrease in oxidation efficiency upon the introduction of $K_2Cr_2O_7$, highlighting the importance of electrons in generating $\bullet O_2^-$ radicals critical for NO to NO_3^- conversion. The addition of PBQ, which also led to a marked decrease in photocatalytic activity, reaffirmed the role of $\bullet O_2^-$ radicals in NO oxidation. Conversely, KI had a moderate impact on the efficiency, suggesting a less but noticeable contribution of holes in the oxidation process. Meanwhile, IPA displayed minimal effect on the photocatalytic efficiency, confirming that hydroxyl radicals play a smaller role, likely due to their lower oxidative potential compared to other ROS. These findings suggest that the radical trapping experiments provide compelling evidence that the photocatalytic oxidation of NO in this composite is predominantly driven by the conduction band activities, with both e^- and $\bullet O_2^-$ playing pivotal roles. The overall process is thus characterized by a higher dependency on the reactions occurring on the conduction band rather than the valence band, outlining a clear pathway for NO degradation in the studied photocatalytic system.

EPR spectroscopy was employed to investigate the generation of ROS during the photocatalytic process. The spectra, as delineated in Fig. 7(a-b), display the signal intensity for DMPO-$\bullet O_2^-$and DMPO-•OH adducts,

Table 1
Comparison of photocatalytic efficiency with previous research.

Photocatalyst	Catalyst dosage/mg	Initial NO concentration ppb	Light source	Efficiency %	Year	Reference
CNT-12	100	400	300 W Xe lamp	32.8	2019	[34]
gCN-NSs	200	600	420 nm LED lamp	35.83	2019	[35]
Au@CN	200	550	150 W lamp	41	2019	[36]
CH-H-600	100	600	150 W lamp	41.84	2020	[37]
DCN-O-R	50	800	300 W Xe lamp	45	2023	[38]
40TAPPy-DMTP-COF	200	800	300 W Xe lamp	45.8	2024	This study
N-TiO_2/g-C_3N_4	200	600	300 W Xe lamp	46.1	2018	[39]
Bi@BiOBr/C	50	800	300 W Xe lamp	69.5	2024	[40]
Bi/BiOBr	50	800	300 W Xe lamp	63	2023	[41]

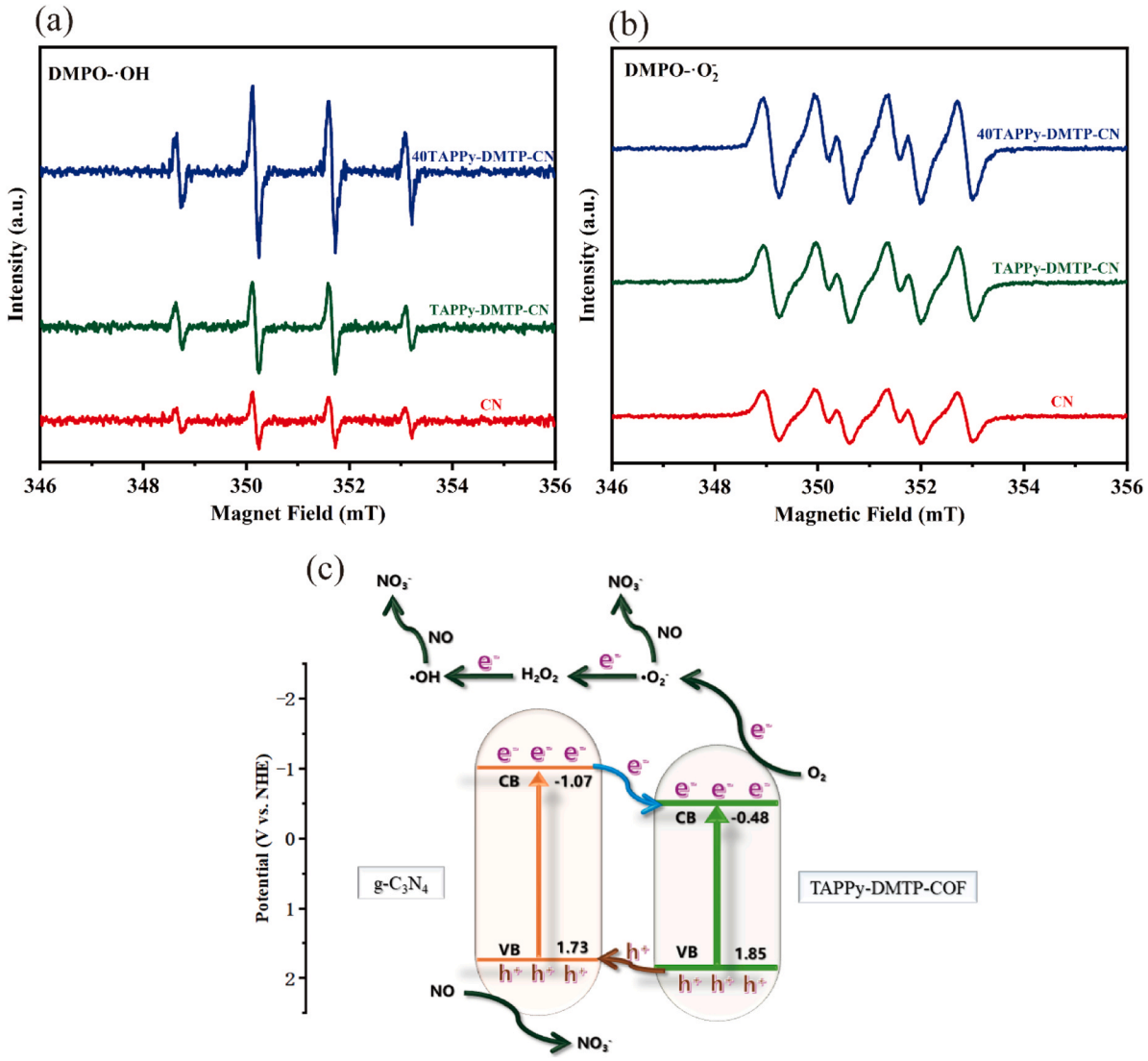

Fig. 7. EPR signals of CN, TAPPy-DMTP-CN and 40TAPPy-DMTP-CN for •OH (a) and $•O_2^-$ (b), (c) the photocatalytic oxidation mechanism of NO on 40TAPPy-DMTPP-COF.

respectively, which are indicative of superoxide and hydroxyl radical presence. For the DMPO-•OH adducts (Fig. 7(a)), the composite's spectrum for DMPO-•OH adducts showed the most intense signals, indicating a significant hydroxyl radical presence. Similarly, the 40TAPPy-DMTP-CN composite (Fig. 7(b)) exhibited notably stronger EPR signals of $•O_2^-$ compared to the individual components, TAPPy-DMTP-COF and CN, suggesting enhanced superoxide radical production. These pronounced EPR signals in the 40TAPPy-DMTP-CN highlight its exceptional ROS generation capacity, crucial for the effective photocatalytic oxidation of NO. The superior generation of ROS by this composite underscores the efficient charge separation and transfer facilitated by the heterojunction between TAPPy-DMTP-COF and CN. This structural synergy effectively impedes electron-hole recombination, enhancing the availability of photogenerated electrons and holes to participate in NO oxidation.

In our investigation, the design and synthesis of a covalently connected Type-II heterostructure have been meticulously executed to enhance photocatalytic activity. Detailed XPS analysis has confirmed electron dynamics, highlighting a decrease in peak energy for TAPPy-DMTP-COF within the TAPPy-DMTP-CN composite, indicative of an increase in electron density and validating electron transfer from CN to TAPPy-DMTP-COF. Consequently, electrons from the CB of CN spontaneously transferred to the CB of TAPPy-DMTP-COF, while the photogenerated holes transfer from VB of TAPPy-DMTP-COF to VB of CN. The transfer mechanism leads to VB of CN and the CB of TAPPy-DMTP-COF became enriched with redox-active charge carriers, facilitating the photocatalytic oxidation of NO.

During photocatalytic activity (Fig. 6(c)), molecular oxygen is initially adsorbed onto the photocatalyst's surface, where it readily interacts with photogenerated electrons in the CB of TAPPy-DMTP-COF (-0.48 eV) to form $•O_2^-$ [42]. This interaction instigates a significant oxidative activation on the photocatalyst's surface, where the $•O_2^-$ radicals either directly oxidize NO to NO_3^- or further accept electrons to transform into •OH, despite their less dominant role in the photocatalytic oxidation of NO. Conversely, the VB of CN exhibits a lower oxidative potential (1.85 eV), insufficient to oxidize H_2O to •OH directly [43]. Instead, the accumulated h^+ in the VB preferentially engages in the direct oxidation of NO to NO_3^-, which is constituents with trapping experiment result with a substantial reduction in photocatalytic efficiency to 23.4 % upon hole trapping, signifying a vital role for h^+ in the oxidation process. The in-situ growth technique facilitates the formation of TAPPy-DMTP-COF directly on the surface of CN by chemical bond, establishing a foundation for enhanced photocatalytic activity through a Type-II heterojunction mechanism. In this configuration, electrons are

transferred from the CN to the surface linked TAPPy-DMTP-COF, thereby localizing oxidative species at TAPPy-DMTP-COF and positioning it as the central active site for facilitating photocatalytic oxidation reactions. This electron transfer dynamically enriches the COF's role in the photocatalytic process, enhancing its efficacy in driving oxidation reactions. Furthermore, the intrinsic porous architecture of the COF, combined with its strong light absorption capabilities, significantly improves the adsorption of light, NO, and O_2. These attributes synergistically amplify the photocatalytic oxidation efficiency, underscoring the COF's dominance as a potent active site which further confirmed the critical role of electron and $\bullet O_2^-$ in trapping experiment. During the photocatalytic oxidation of NO, the production of NO_2 is a transient intermediate resulting from the reaction of NO with ROS generated by the photocatalyst under light irradiation. The initial oxidation of NO by superoxide radical produces NO_2, which can be further oxidized to NO_3^- through reactions with hydroxyl radicals. The intermediate accumulation of NO_2 depends on the availability of ROS, the efficiency of the photocatalyst, and reaction conditions. Thus, the presence of NO_2 in the g-C_3N_4 sample predominantly arises from deficient ROS generation, primarily due to the rapid recombination of electron-hole pairs. This impedes the effective participation of photogenerated electrons and holes in the photocatalytic oxidation process. Conversely, the 40TAPPy-DMTP-CN exhibits better photoelectrochemical properties, possesses a 97.4 % NO_3^- selectivity with very low conversion efficiency for NO_2 through the above mentioned oxidation pathway [44].

Furthermore, the intrinsic porous architecture of the COF, coupled with its strong light absorption capabilities, significantly boosts the adsorption of light, NO, and O_2. These attributes synergistically enhance the photocatalytic oxidation efficiency, highlighting the COF's dominance as a potent active site. This intricately engineered mechanism within the Type-II architecture not only positions TAPPy-DMTP-COF as the principal active site on the surface of CN but also introduces a rapid electron transfer route through chemical bonding. These mechanistic insights into the covalently connected Type-II heterostructure illustrate the dual roles of electrons and $\bullet O_2^-$ in enhancing photocatalytic degradation of NO, emphasizing the importance of meticulously engineered photocatalytic systems for effective environmental remediation.

4. Conclusion

In this research, we have optimized the structure of a pyrene-based COF and synthesized a covalently linked Type-II TAPPy-DMTP-COF/CN heterostructure, aiming to significantly enhance the photocatalytic performance. This enhancement is achieved through the in-situ formation of TAPPy-DMTP-COF on the surface of CN via Schiff-base reactions, which ensures robust electron communication between the two components. The enhanced electron communication is confirmed by both XPS and photoelectrochemical results. Remarkably, the 40TAPPy-DMTP-COF variant has exhibited unparalleled photocatalytic efficiency, achieving a 45.8 % removal rate of NO under visible light conditions. The synergistic interaction between TAPPy-DMTP-COF and CN, pivotal to this composite's effectiveness, has been thoroughly validated through photoelectrochemical characterization and comprehensive photocatalytic activity assays. Additionally, the superior generation of ROS by this composite underscores the efficient charge separation and transfer facilitated by the heterojunction between TAPPy-DMTP-COF and CN. This structural synergy effectively impedes electron-hole recombination, enhancing the availability of photogenerated electrons and holes to participate in NO oxidation. Within this heterostructure, TAPPy-DMTP-COF serves as a main active site growth on the surface of CN. Its pronounced porous structure and superior light absorption capabilities markedly elevate the photocatalytic oxidation efficiency for NO removal. Moreover, the 40TAPPy-DMTP-CN composite not only showcases an impressive 97.4 % selectivity towards NO_3^- formation but also maintains exceptional stability, as evidenced by its consistent performance across a 600-minute cyclic experiment. This research not only precisely controls the structural length and functional group addition of pyrene-based COFs but also introduces a novel approach for enhancing NO oxidation. By constructing a covalently linked Type-II heterostructure, we have significantly improved the interface interaction within the heterostructure, resulting in superior photocatalytic performance. Consequently, this study underscores the potential of carefully engineered COF heterostructures in advancing the photocatalytic oxidation of NO, providing a novel pathway for COF design.

CRediT authorship contribution statement

George Chen: Writing – review & editing, Supervision. **Yong Ren:** Writing – review & editing. **Zhiyu Xiao:** Writing – original draft, Methodology, Investigation, Data curation, Conceptualization. **Jun He:** Writing – review & editing, Resources, Project administration, Funding acquisition. **Chengjun Wang:** Visualization, Validation, Formal analysis. **Yong Sun:** Writing – review & editing, Supervision.

Declaration of Competing Interest

The authors declare the following financial interests/personal relationships which may be considered as potential competing interests: Jun He reports financial support was provided by Ningbo Bureau of Science and Technology. If there are other authors, they declare that they have no known competing financial interests or personal relationships that could have appeared to influence the work reported in this paper.

Data Availability

Data will be made available on request.

Acknowledgements

This work was jointly sponsored by the Ningbo Science and Technology Innovation Key Project (2022Z028), Ningbo Natural Science Foundation Grant (2023J024), Ningbo Commonweal Key Research Program (2023S038) and Ningbo Key Technology Breakthrough Scheme Projects under Yongjiang Science and Innovation 2035 (2024Z237, 2024Z251).

References

[1] X. Zhao, P. Pachfule, A. Thomas, Covalent organic frameworks (COFs) for electrochemical applications, Chem. Soc. Rev. 50 (2021) 6871–6913.
[2] S. Ghasemi, M. Nazari, M. Padervand, A. Labidi, E.A. Dawi, M. Signoretto, T. Hamzehlouyan, C. Wang, Chapter 15 - Organic radicals: formation, classification, and environmental application, in: C. Wang, A. Labidi, E. Lichtfouse (Eds.), Organic Radicals, Elsevier, 2024, pp. 393–412.
[3] U. Shahzad, H.M. Marwani, M. Saeed, A.M. Asiri, M.R. Repon, R.H. Althomali, M. M. Rahman, Progress and perspectives on promising Covalent-Organic Frameworks (COFs) materials for energy storage capacity, Chem. Rec. 24 (2024) e202300285.
[4] A. Shahbaz, K. Ahmad, K. Qureshi, H. Majeed, I. Arshad, T. Tabinda, T. Iftikhar, K.-U. Khair, M. Ashfaq, H.U.R. Shah, M.Z. Ahmad, S.-L. Lee, Porous materials: Covalent Organic Frameworks (COFs) as game-changers in practical applications, a review, Rev. Inorg. Chem. 44 (2024) 117–133.
[5] S.-P. Qi, R.-T. Guo, Z.-X. Bi, Z.-R. Zhang, C.-F. Li, W.-G. Pan, Recent progress of Covalent Organic frameworks-based materials in photocatalytic applications: a review, Small 19 (2023) 2303632.
[6] Q. Yang, M. Luo, K. Liu, H. Cao, H. Yan, Covalent organic frameworks for photocatalytic applications, Appl. Catal. B Environ. 276 (2020) 119174.
[7] J. Sun, H. Sekhar Jena, C. Krishnaraj, K. Singh Rawat, S. Abednatanzi, J. Chakraborty, A. Laemont, W. Liu, H. Chen, Y.-Y. Liu, K. Leus, H. Vrielinck, V. Van Speybroeck, P. Van Der Voort, Pyrene-based covalent organic frameworks for photocatalytic hydrogen peroxide production, Angew. Chem. Int. Ed. 62 (2023) e202216719.
[8] X. Dong, F. Zhang, F. Huang, X. Lang, Pyrene-based conjugated microporous polymers for red light-powered oxidation of amines to imines, Appl. Catal. B Environ. 318 (2022) 121875.

[9] Z. Hu, Y. Luo, L. Wang, Y. Wang, Q. Wang, G. Jiang, Q. Zhang, F. Cui, Synthesis of Pyrene-based covalent organic frameworks for photocatalytic tetracycline degradation, ACS Appl. Polym. Mater. 5 (2023) 9263–9273.
[10] G.T.V.P.H.T. Philipsen, E.J. Baerends, J.A. Berger, P.L. de Boeij, M. Franchini, J.A. Groeneveld, E.S. Kadantsev, R. Klooster, F. Kootstra, P. Romaniello, M. Raupach, D.G. Skachkov, J.G. Snijders, C.J.O. Verzijl, J.A. Celis Gil, J.M. Thijssen, G. Wiesenekker, T. Ziegler, BAND202, SCM, Theoretical Chemistry, Vrije Universiteit, Amsterdam, The Netherlands.
[11] X. Deng, N. Gao, L. Bai, Bromine Atoms Decorated Pyene-based Covalent Organic Frameworks for Accelerated Photocatalytic H2 Production, Small, n/a 2311927.
[12] L. Stegbauer, S. Zech, G. Savasci, T. Banerjee, F. Podjaski, K. Schwinghammer, C. Ochsenfeld, B.V. Lotsch, Tailor-made photoconductive pyrene-based covalent organic frameworks for visible-light driven hydrogen generation, Adv. Energy Mater. 8 (2018) 1703278.
[13] Z. Xiao, H. Do, A. Yusuf, H. Jia, H. Ma, S. Jiang, J. Li, Y. Sun, C. Wang, Y. Ren, G. Z. Chen, J. He, Facile synthesis of multi-layer $Co(OH)_2/CeO_2$-g-C_3N_4 ternary synergistic heterostructure for efficient photocatalytic oxidation of NO under visible light, J. Hazard. Mater. 462 (2024) 132744.
[14] Y. Xia, H. Yang, W. Ho, B. Zhu, J. Yu, Promoting the photocatalytic NO oxidation activity of hierarchical porous g-C_3N_4 by introduction of nitrogen vacancies and charge channels, Appl. Catal. B Environ. Energy 344 (2024) 123604.
[15] H. Han, X. Wang, Y. Qiao, Y. Lai, B. Liu, Y. Zhang, J. Luo, S. Toan, L. Wang, Construction of S-scheme heterojunction for enhanced photocatalytic conversation of NO over dual-defect CeO_{2-x}/g-$C3N_{4-x}$, J. Alloy. Compd. 933 (2023) 167819.
[16] J. Liu, X. Huang, L. Hu, P. Liu, L. Jia, K. Sasaki, Z. Tan, H. Yu, Nitric oxide removal by synergistic photooxidation and adsorption using Pd_1/g-C_3N_4-UiO-66-NH_2 P-A heterojunction, Chem. Eng. J. 476 (2023) 146768.
[17] X. Zhang, H.S. Chen, S.P. Jiang, P. Yang, $W_{18}O_{49}$/crystalline g-C_3N_4 layered heterostructures with full solar energy harvesting towards efficient H_2O_2 generation and NO conversion, Nano Energy 120 (2024) 109160.
[18] L. Wang, R. Lian, Y. Zhang, X. Ma, J. Huang, H. She, C. Liu, Q. Wang, Rational preparation of cocoon-like g-C_3N_4/COF hybrids: accelerated intramolecular charge delivery for photocatalytic hydrogen evolution, Appl. Catal. B Environ. 315 (2022) 121568.
[19] T.D. Kühne, M. Iannuzzi, M. Del Ben, V.V. Rybkin, P. Seewald, F. Stein, T. Laino, R. Z. Khaliullin, O. Schütt, F. Schiffmann, D. Golze, J. Wilhelm, S. Chulkov, M. H. Bani-Hashemian, V. Weber, U. Borštnik, M. Taillefumier, A.S. Jakobovits, A. Lazzaro, H. Pabst, T. Müller, R. Schade, M. Guidon, S. Andermatt, N. Holmberg, G.K. Schenter, A. Hehn, A. Bussy, F. Belleflamme, G. Tabacchi, A. Glöß, M. Lass, I. Bethune, C.J. Mundy, C. Plessl, M. Watkins, J. VandeVondele, M. Krack, J. Hutter, CP2K: An electronic structure and molecular dynamics software package - Quickstep: efficient and accurate electronic structure calculations, The, J. Chem. Phys. 152 (2020).
[20] Z. Zhou, C. Bie, P. Li, B. Tan, Y. Shen, A thioether-functionalized pyrene-based covalent organic framework anchoring ultrafine Au nanoparticles for efficient photocatalytic hydrogen generation, Chin. J. Catal. 43 (2022) 2699–2707.
[21] Z. Yang, M. Yuan, Z. Cheng, B. Liu, Z. Ma, J. Ma, J. Zhang, X. Ma, Pa Ma, J. Lin, Defect-Repaired g-C3N4 Nanosheets: Elevating the Efficacy of Sonodynamic Cancer Therapy Through Enhanced Charge Carrier Migration, Angewandte Chemie International Edition, n/a e202401758.
[22] J. Tang, Z. Liang, H. Qin, X. Liu, B. Zhai, Z. Su, Q. Liu, H. Lei, K. Liu, C. Zhao, R. Cao, Y. Fang, Large-area free-standing metalloporphyrin-based covalent organic framework films by liquid-air interfacial polymerization for oxygen electrocatalysis, Angew. Chem. Int. Ed. 62 (2023) e202214449.
[23] S. Wu, C. Li, Y. Wang, Y. Zhuang, Y. Pan, N. Wen, S. Wang, Z. Zhang, Z. Ding, R. Yuan, W. Dai, X. Fu, J. Long, The Keto-switched photocatalysis of reconstructed covalent organic frameworks for efficient hydrogen evolution, Angew. Chem. Int. Ed. 62 (2023) e202309026.
[24] H. Lu, X. Li, Y. Jiang, X. Hu, S. Zhou, H. Sun, D. Zou, Y. Liang, X. Gong, Z. Wu, Natural sunlight driven degradation of tetracycline in wastewater by dual Z − scheme photocatalyst of hollow nanospherical β–In_2S_3 decorated g − C3N4/WO3: performance, mechanism and products toxicity, Chem. Eng. J. 476 (2023) 146718.
[25] C. Feng, X. Ouyang, Y. Deng, J. Wang, L. Tang, A novel g-C_3N_4/g-C_3N_{4-x} homojunction with efficient interfacial charge transfer for photocatalytic degradation of atrazine and tetracycline, J. Hazard. Mater. 441 (2023) 129845.
[26] M. Jiang, Y. Wang, H. Liu, S. Yu, K.-K. Niu, L.-B. Xing, Construction of a novel pyrene-based two-dimensional supramolecular organic framework and the selective regulation of reactive oxygen species for photocatalysis, J. Mater. Chem. A 12 (2024) 4752–4760.
[27] D. Tan, F. Huang, S. Guo, D. Li, Y. Yan, W. Zhang, Efficient photocatalytic tetracycline elimination over Z-scheme g-C_3N_4/Bi_5O_7I heterojunction under sunshine light: performance, mechanism, DFT calculation and pathway, J. Alloy. Compd. 946 (2023) 169468.
[28] H.-Y. Yu, J.-S. Wang, F.-Y. Xie, Q. Yang, Y. Chen, L. Zhao, Y. Li, W.-J. Ruan, A stack-guiding unit constructed 2D COF with improved charge carrier transport and versatile photocatalytic functions, Chem. Eng. J. 445 (2022) 136713.
[29] D. Yadav, A. Kumar, J.Y. Kim, N.-J. Park, J.-O. Baeg, Interfacially synthesized 2D COF thin film photocatalyst: efficient photocatalyst for solar formic acid production from CO_2 and fine chemical synthesis, J. Mater. Chem. A 9 (2021) 9573–9580.
[30] F. Dong, Z. Zhao, T. Xiong, Z. Ni, W. Zhang, Y. Sun, W.-K. Ho, In situ construction of g-C_3N_4/g-C_3N_4 metal-free heterojunction for enhanced visible-light photocatalysis, ACS Appl. Mater. Interfaces 5 (2013) 11392–11401.
[31] H. Che, C. Li, C. Li, C. Liu, H. Dong, X. Song, Benzoyl isothiocyanate as a precursor to design of ultrathin and high-crystalline g-C_3N_4-based donor–acceptor conjugated copolymers for superior photocatalytic H_2 production, Chem. Eng. J. 410 (2021) 127791.
[32] S. Gao, X. Wang, C. Song, S. Zhou, F. Yang, Y. Kong, Engineering carbon-defects on ultrathin g-C_3N_4 allows one-pot output and dramatically boosts photoredox catalytic activity, Appl. Catal. B Environ. 295 (2021) 120272.
[33] C. Wu, S. Xue, Z. Qin, M. Nazari, G. Yang, S. Yue, T. Tong, H. Ghasemi, F.C. R. Hernandez, S. Xue, D. Zhang, H. Wang, Z.M. Wang, S. Pu, J. Bao, Making g-C_3N_4 ultra-thin nanosheets active for photocatalytic overall water splitting, Appl. Catal. B Environ. 282 (2021) 119557.
[34] Z. Wang, Y. Huang, M. Chen, X. Shi, Y. Zhang, J. Cao, W. Ho, S.C. Lee, Roles of N-vacancies over porous g-C_3N_4 microtubes during photocatalytic NOx removal, ACS Appl. Mater. Interfaces 11 (2019) 10651–10662.
[35] X. Wu, J. Cheng, X. Li, Y. Li, K. Lv, Enhanced visible photocatalytic oxidation of NO by repeated calcination of g-C_3N_4, Appl. Surf. Sci. 465 (2019) 1037–1046.
[36] K. Li, W. Cui, J. Li, Y. Sun, Y. Chu, G. Jiang, Y. Zhou, Y. Zhang, F. Dong, Tuning the reaction pathway of photocatalytic NO oxidation process to control the secondary pollution on monodisperse Au nanoparticles@g-C_3N_4, Chem. Eng. J. 378 (2019) 122184.
[37] J. Liao, W. Cui, J. Li, J. Sheng, H. Wang, Xa Dong, P. Chen, G. Jiang, Z. Wang, F. Dong, Nitrogen defect structure and NO^+ intermediate promoted photocatalytic NO removal on H_2 treated g-C_3N_4, Chem. Eng. J. 379 (2020) 122282.
[38] H. Wang, X. Xu, A. Labidi, H. Ren, A.A. Allam, A. Rady, Y. Huang, S. Wei, M. Padervand, S. Ghasemi, C. Wang, Cyano/hydroxyl groups Co-functionalized g-C_3N_4 for photocatalytic NO removal: a synergistic strategy towards inhibition of toxic intermediate NO_2, Catalysts 13 (2023) 1433.
[39] G. Jiang, J. Cao, M. Chen, X. Zhang, F. Dong, Photocatalytic NO oxidation on N-doped TiO_2/g-C_3N_4 heterojunction: enhanced efficiency, mechanism and reaction pathway, Appl. Surf. Sci. 458 (2018) 77–85.
[40] X. Li, Q. Dong, F. Li, Q. Zhu, Q. Tian, L. Tian, Y. Zhu, B. Pan, M. Padervand, C. Wang, Defective Bi@BiOBr/C microrods derived from Bi-MOF for efficient photocatalytic NO abatement: directional regulation of interfacial charge transfer via carbon–loading, Appl. Catal. B Environ. 340 (2024) 123238.
[41] Y. Xin, Q. Zhu, T. Gao, X. Li, W. Zhang, H. Wang, D. Ji, Y. Huang, M. Padervand, F. Yu, C. Wang, Photocatalytic NO removal over defective Bi/BiOBr nanoflowers: the inhibition of toxic NO_2 intermediate via high humidity, Appl. Catal. B Environ. 324 (2023) 122238.
[42] Y. Tang, W. Cui, S. Wang, F. Dong, Efficient photocatalytic NO removal with inhibited NO_2 formation and catalyst loss over sponge-supported and functionalized g-C_3N_4, J. Hazard. Mater. 465 (2024) 133323.
[43] B. Liu, H. Huang, Z. Xiao, J. Yang, M. Zhu, 2D/3D g-C_3N_4/BiOI heterostructure catalyst for efficient and robust photocatalytic NO removal, Sep. Purif. Technol. 310 (2023) 123183.
[44] H. Wu, C. Yuan, R. Chen, J. Wang, F. Dong, J. Li, Y. Sun, Mechanisms of interfacial charge transfer and photocatalytic NO oxidation on BiOBr/SnO_2 p–n heterojunctions, ACS Appl. Mater. Interfaces 12 (2020) 43741–43749.